

Development of an EAM potential for zinc and its application to the growth of nanoparticles†

F. Römer, S. Braun and T. Kraska*

Received 12th November 2008, Accepted 4th February 2009

First published as an Advance Article on the web 2nd March 2009

DOI: 10.1039/b820278h

In the context of the investigation of particle formation, a potential model by means of the embedded atom method is developed for the hexagonal close packed metal zinc. This type of model includes many-body interactions caused by delocalised electrons in metals. The effective core charge as function of the distance is calculated here by an integral over the electron distribution function rather than fitting it to experimental data. In addition, the dimer potential is included in the parameterisation because we focus on the formation of nanoparticles from the vapour phase. With this potential model, the growth of zinc clusters consisting of 125 to 1000 atoms is investigated, which takes place at elevated temperatures in a liquid-like cluster state. The growing clusters are embedded in an argon carrier gas atmosphere which regulates the cluster temperature. The average thermal expansion of the clusters and the different lattice constants are analysed. For the determination of the cluster structure, the common-neighbour analysis method is extended to hexagonal close packed surface structures. During growth, small clusters with less than approximately 60 atoms develop transient icosahedral structure before transforming into hexagonal close-packed structure. The surface of the clusters exhibits a transformation from planes with high surface energy to the most stable ones. Besides ambiguous surface structures the final clusters are almost completely in an hexagonal close packed structure.

1. Introduction

The synthesis of zinc nanoparticles is of interest from a fundamental as well as an applied point of view. One way to produce zinc particles is vapour phase condensation. The supersaturated vapour can be obtained from evaporation^{1,2} or from decomposition of a precursor gas.³ Such particle synthesis methods are usually investigated based only on the analysis of the resulting particles because it is difficult to monitor the early stages of particle growth experimentally. Therefore, the investigation of the growth of nanoparticles by molecular dynamics simulation is an important contribution to the understanding of their special properties, which differ from those of the bulk material. For example, it is well known that the melting point of nanoparticles is significantly below that of the bulk material.^{4,5} Also the melting and solidification processes of nanoparticles themselves are different to those in the bulk phase.^{6,7} While these effects are related to the large surface–volume ratio of nanoparticles, special electronic effects appear due to the confinement in a small cluster.⁸ Furthermore, local atomic ordering being different from that of the bulk phase such as icosahedral structure can be found.⁹

The interest in zinc nanoparticles and small clusters is twofold: first the formation of zinc clusters starting with homogeneous nucleation¹⁰ followed by growth and structure

formation, as well as their properties, are of interest in a solar process for hydrogen formation.^{11,12} Under certain conditions the reoxidation of zinc can be suppressed to a large extent, leading to zinc clusters. Secondly zinc is a hcp metal with a strong deviation of the lattice constant ratio $c/a = 1.856$ from the ideal value $c/a = 1.63$ corresponding to the close packing fraction 0.74. While potential models have been developed for many fcc metals relatively few papers focus on hcp metals. In case of zinc one can find *ab initio* and DFT investigations of cluster structures and properties,^{8,13,14} experimental investigations,^{15–17} as well as force field developments.^{18–21} *Ab initio* quantum mechanic calculations and DFT calculations typically focus on the structure of clusters at zero Kelvin. While such investigations are important for the understanding of matter they are not suitable for the investigation of particle growth. It is known from experiments^{22,23} and from simulation^{10,24,25} that for metals the critical cluster size is in the order of 2 to 12 atoms. Furthermore, it is known that the temperature of the forming cluster may become very high.^{10,26} Hence, metal clusters are in a liquid-like state undergoing continuous condensation and evaporation of atoms when formed in the vapour phase. Only after cooling down by collisions with a carrier gas they eventually transform into a solid-like state. The advantage of force field models is that one can treat large systems at elevated temperatures including the effects of a carrier gas. However, the force field models for zinc available in the literature are developed for the solid state by using a harmonic approximation. This approximation is valid only for small displacements from the equilibrium position of an atom in the lattice.²⁷ Since we are here interested in the

Institute for Physical Chemistry, University Cologne, Luxemburger Str. 116, D-50939 Köln, Germany. E-mail: t.kraska@uni-koeln.de

† Electronic supplementary information (ESI) available: Fit parameters of the zinc EAM potential; CNA signatures for the hcp structure. See DOI: 10.1039/b820278h

growth of nanoparticles and their properties, which requires a potential model valid for the bulk phase on one side, as well as for the zinc dimer on the other side, we have developed a new parameterization of the embedded atom method (EAM) for zinc. EAM is a widely used potential model for metals^{28–30} and it has been proven to be applicable to nanoparticles, even in cases where it has been fitted to bulk properties only.³¹ The input for the potential model optimisation comprises quantum mechanical information, structure, energies, and macroscopic mechanical properties of zinc.

2. Method

2.1 Potential model development

For the application in vapour phase nucleation and growth a potential model is required which is able to describe the bulk phase as well as the vapour phase at high temperature. There are few potential models for zinc available that do not fulfil these requirements. In the model of Igarashi *et al.*,²⁰ for example, the embedding energy is optimized using experimental data of the mechanical properties of the bulk only. It is then expanded in a series around the equilibrium distance limiting its applicability to the solid bulk phase. Furthermore, it is optimized for room temperature and below. Another model³² distinguishes two types of zinc atoms depending on the layer in that they are located. Such approach is also not suitable to investigate the growth of zinc particles from the vapour phase. Therefore we have developed a new parameterization of the embedded atom method (EAM) which takes into account the dimer properties. It is known that the inclusion of the dimer properties is not necessarily required to get the correct nanoparticles structures.^{31,33–35} Therefore it has been seldom accounted for in effective medium models and rarely applied, typically in systems where surfaces are important.³⁶ That is however not always necessary. For example, it has been shown for silver that surface energies can be described well by EAM, even without the inclusion of dimer properties.³⁷ Still including the dimer properties in the potential development can improve the representation of small clusters.³⁴ We take the dimer properties into account in order to get the limiting behaviour of the vapour phase correct because we are interested in the growth from the vapour phase.

The embedded atom method (EAM) consists of two terms: one term describes the delocalised electrons by a many-body term as a functional F_i of the local host electron density $\rho_{h,i}(r_i)$; the second term is a pairwise additive repulsive term $\phi_{ij}(r_{ij})$ of the atomic cores:

$$E_{\text{EAM}} = \sum_{i=1}^N F_i[\rho_{h,i}(r_i)] + \frac{1}{2} \sum_{\substack{ij \\ j \neq i}}^N \phi_{ij}(r_{ij}) \quad (1)$$

$$\rho_{h,i}(r_i) = \sum_{j \neq i}^N \rho_j^{\text{at}}(r_{ij}) \quad (2)$$

The local electron density is the sum of the contributions of ρ_j^{at} for all atoms in the interaction range. The many-body functional effectively accounts for the effect of different coordination numbers, since it depends on the local electron

density. This potential model consists of several functions such as the electron density distribution, the effective core charge and the embedding function. The development of these functions is described in this section.

The electron density distribution. The atomic system is separated into the core and the valence electrons. First a function for the radial valence electron distribution is required. For this function we employ the expressions of Clementi *et al.*³⁸ for free atoms, which have been obtained with the single-determinant Hartree–Fock theory. Since the electron configuration differs between free atoms and bulk atoms, Daw and Baskes²⁹ introduced a parameter taking into account the natural population of the valence orbitals. Zinc ($3d^{10}4s^2$) is a closed shell system, hence a detailed investigation about the s-character is not necessary since there is no remarkable shift from the 4s-electrons to vacant orbitals. DFT studies of small zinc clusters ($N \leq 32$) predict an average shift of not more than 0.2 electrons to the 4p orbital,³⁹ which has no significant effect on the distribution function in the relevant region. On the other hand, recent DFT calculations of zinc in the bulk phase show that within the DFT approach the d-shell is necessary in order to get a reasonable value for the c/a ratio. Omitting the d-shell gives a c/a value of 1.57 which is even smaller than the ideal value.⁴⁰ Including the 3d-electrons as valence electrons leads to a very high core charge and hence to very steep core–core repulsion within the effective EAM approach leading to worse agreement with the experimental data of the caloric and the mechanical properties. The dimer properties and the bulk properties cannot be simultaneously well-described if the 3d-orbitals are included in the valence electrons. A possible reason is that the mapping of the 3d-electrons on a radial electron distribution leads to inaccuracies, which is not the case for the 4s-electrons. Therefore, within the effective medium approach of EAM we here use the minimum valence Ansatz ($4s^2$) and associate the closed 3d-shell with the core as it has been done in the literature.²⁷

The electron density distribution of a zinc atom ρ_j^{at} is calculated by eqn (3) from the wave-function of the 4s-electrons.³⁸

$$\rho_j^{\text{at}}(r) = 2 \cdot |\psi_{4s}|^2 \quad (3)$$

The factor 2 accounts for two s-electrons. In order to reduce the complexity of the model we describe the atomic electron distribution by a two-parameter exponential function as suggested by Oh and Johnson²⁷ and fit it to eqn (3):

$$\rho_j^{\text{at}}(r) \equiv f_e e^{-\beta(r/r_e-1)} \quad (4)$$

The parameters of eqn (4) are listed in Table 1 in the ESI.† The obtained function is in good agreement with first principle calculation down to a distance of 0.15 nm (Fig. 1a) which is a sufficient range.

The effective core charge. In the classic EAM the repulsive core-core potential is described by the Coulomb interaction between two screened charges:

$$\phi_{ij}(r_{ij}) = \frac{Z_i(r_{ij}) \cdot Z_j(r_{ij})}{r_{ij}} \quad (5)$$

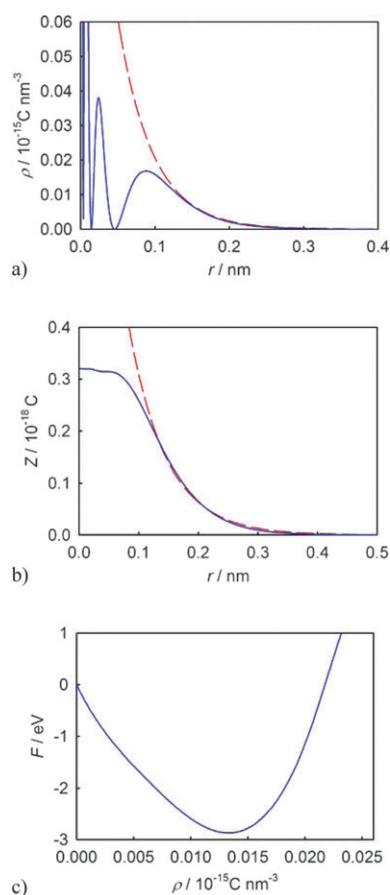


Fig. 1 (a) Electron density distribution as function of the distance. (b) Screened core charge Z as function of the distance. (c) Embedding energy F as function of the local electron density. In (a) and (b) the solid (blue) curves represents the calculated value and the dashed (red) curve the fitting functions (eqn (4) and (7)), that are used in the potential.

Table 1 Lattice parameters⁵² of zinc used in the fit procedure

Parameter	Value
a/nm	0.2665
c/a	1.856
Ω_e/nm^3	0.011263
r_c/nm	0.635

The screened charges are expressed as effective core charges depending on the distance. Here we propose an expression for this effective core charge, which is derived from the radial electron distribution without any empirical adjustment. It provides a solid link between the repulsive pair potential and the embedding function. This is important to avoid a shift of the energy between the embedding function and the repulsive pair potential during the correlation procedure.⁴¹ It makes the correlation more stable and avoids artificial compensations during fitting. The effective core charge Z in a distance r is calculated from the plain core ($\text{Zn}^{2+} \cdot [\text{Ar}]3\text{d}^{10}$) charge $Z_0 = 2$ reduced by the partial charge of the valence electrons integrated up to radius r . This screening is obtained from

an integral over the electron density distribution function calculated from eqn (3):

$$Z(r) = Z_0 - \int_0^r \rho^{\text{at}}(r) \cdot 4\pi r^2 dr \quad (6)$$

It is interesting to note that the inclusion of a freely adjustable screened core charge in a generic fitting to experimental data and the function of Rose *et al.* mentioned later in this article (eqn (9)), leads to a function, which agrees well with that obtained from the eqn (6). To be consistent⁴² with the electron density distribution, the results of eqn (6) are also fitted to a two parameter exponential function:

$$Z(r) \equiv Z_c \cdot e^{-\alpha(r/r_c-1)} \quad (7)$$

The comparison of both screened core charges is shown in Fig. 1b.

The embedding function. The energy of the delocalised electrons as function of the local electron density is calculated by the embedding function F . We obtain the value of F , the gradient $\partial F/\partial \rho$, and the curvature $\partial^2 F/\partial \rho^2$ of the embedding function at the bulk equilibrium electron density ρ_e by fitting with caloric and mechanical properties. For calculating the elastic constants, we use the equations given by Johnson.⁴³ The cohesive energy per atom is then described within EAM⁴⁴ by

$$E_{c,\text{EAM}} = F(\rho) + \frac{1}{2} \sum_{j \neq i}^N \phi(r_{ij}) \quad (8)$$

From the universal function for metals from Rose *et al.*⁴⁵ (eqn (9)) we extract information about the devolution of the function for short distances smaller than r_c , far away from the equilibrium.⁴⁶

$$E_{c,\text{Rose}}(x^*) = -E_{c,e}(1+x^*)e^{-x^*} \quad \text{with } x^* = \frac{x/a-1}{\sqrt{\frac{-E_{c,e}}{9B\Omega_e}}} \quad (9)$$

Here x is a variable lattice constant and a is its equilibrium value in bulk. $E_{c,e}$ is the cohesive energy in the lattice at equilibrium distance r_e . Rose *et al.*⁴⁵ introduced a reduced lattice constant x^* , which also depends on the bulk modulus B and the atomic equilibrium volume Ω_e (Table 1 and ESI Table 1†). Consistent with Puska *et al.*⁴⁷ we adopt for high electron density ($\rho > \rho_{\text{max}}$) a linear ρ_j^{at} . For electron densities lower than ρ_e , we propose a harmonic approach. Hence, the embedding function (Fig. 1c) is represented here by three equations:

$$F(\rho) = \begin{cases} 0 \leq \rho < \rho_e & : \rho \{ F_{a0} + F_{a1}[\rho - \rho_e] + F_{a2}[\rho - \rho_e]^2 \} \\ \rho_e \leq \rho \leq \rho_{\text{max}} & : F_{b0} + F_{b1}[\rho - \rho_e] + \frac{1}{2} F_{b2}[\rho - \rho_e]^2 + F_{b3}[\rho - \rho_e]^3 \\ \rho_{\text{max}} < \rho & : F(\rho_{\text{max}}) + F_{c0}[\rho - \rho_{\text{max}}] \end{cases} \quad (10)$$

The parameters F_{a0} , F_{a1} , F_{a2} , and F_{b0} , F_{b1} , F_{b2} are calculated from the correlation of F and its first two derivatives by fitting to caloric and mechanical properties around the equilibrium distance (ESI Table 1†). The parameter F_{b3} is obtained by a least square fit to the gradient of the Rose function (eqn (9)) to take into account the development far away from the

equilibrium at short distance. The value of r_e , the equilibrium distance to the next-neighbour, is given by the lattice constant a in a hcp system (Table 1).

The cut-off radius of the potential model is $r_c = 0.635$ nm, which is more than twice the lattice constant a and includes 9 neighbourhood shells in the bulk state. It is necessary to choose such large cut-off radius in order to reproduce the cohesive energy correctly. EAM potential models take into account the second moment of the electronic density of states. In order to obtain a hcp structure, one can either use a model which includes up to the sixth moment of the density of states requiring only the next-neighbour shell,⁴⁸ or include at least three neighbour shells because energetic differences between hcp and fcc show up in the third coordination shell.⁴⁹ To implement the cut-off we modify the core charge and electron density function as:

$$h_{\text{smooth}}(r) = \begin{cases} 0 \leq r < r_c & : h(r) - h(r_c) + \left(\frac{r}{r_c}\right) \cdot \left[1 - \left(\frac{r}{r_c}\right)^q\right] \cdot h'(r_c) \\ r_c \leq r & : 0 \end{cases} \quad (11a)$$

$$h(r_c) \ll 0.001 \cdot h_{\text{min}} \quad (11b)$$

Here h represents the unmodified function of either the core charge or the electron density without any cut-off and h_{smooth} is the corresponding modified function with a cut-off at r_c . The parameter q controls the rigidity of the modulation. This expression gives a smooth cut-off, *i.e.* the function itself and the first derivative vary continuously.⁵⁰ For a good balance between a not too strong modification of the original potential and the smoothness of the function the value $q = 20$ is chosen.⁵⁰

The zinc potential model (ESI Table 1†) developed here is in good agreement with the experimental data (Table 2). The systematic overestimation of the higher elastic constants is caused by the limits of EAM in general and is not relevant for growth.⁵¹ In Fig. 2a the cohesive energy of one atom in a hcp bulk phase is plotted *versus* the distance to the next-neighbour for constant c/a ratio as well as the effective pair potential Φ_{eff} of a dimer in vacuum. The dependency of the cohesive energy on the c/a ratio is shown in Fig. 2b. The potential model predicts a smaller equilibrium distance for the dimer than for the bulk state, which is in agreement with experimental data.^{52,53} The experimental c/a ratio in the bulk phase 1.856⁵² is very close to the potential minimum of our model at $c/a = 1.825$.

Table 2 Properties of the zinc potential: the cohesive energy E_c and the elastic constants C_{ij} for the bulk phase and the distance r_2 and the dissociation energy D_0 of the dimer in the vapour phase

Parameter	Experimental	EAM
E_c/eV	-1.3 ⁶⁸	-1.3
C_{11}/GPa	179 ⁶⁸	179
C_{12}/GPa	38 ⁶⁸	47
C_{13}/GPa	55 ⁶⁸	30
C_{33}/GPa	69 ⁶⁸	158
C_{44}/GPa	46 ⁶⁸	61
B/GPa	80 ⁶⁸	81
r_2/nm	0.235 ⁵³	0.237
D_0/eV	0.168 ⁵³	0.190

In order to proof the stability of the hcp structure we have run simulations of bulk-like hcp blocks containing 686 to 2662 atoms from 50 K to 300 K. The reason not to use a bulk phase in the sense of a completely filled simulation box with periodic boundary condition is to avoid a possible bias by the box geometry. It is known that a cubic geometry forces the system into a cubic structure as well as a hexagonal geometry forces the system into a hexagonal one.⁵⁴ To place a block in a vapour phase is hence an unbiased method because there is no stress acting on the system. The unavoidable surface effect can be extracted by using different block sizes, especially large ones. The hcp structure is stable with a small amount of fcc structure as a result of stacking faults caused by some reorganisation taking place in the surface. For increasing size of the bulk-like hcp block there is no change in the stability of the hcp phase. With increasing temperature the hcp structure remains stable until the block melts. Simulations at the same conditions but with an initial fcc structure show a rapid transformation into hcp structure.

In addition, we have performed DFT calculations for small clusters ($N \leq 57$) at MPW1PW91/LanL2DZ level³⁹ in order to compare the results with calculations from the EAM model at zero Kelvin. The results of the DFT calculations are listed in Table 3. Since the icosahedral and hcp clusters have different closed shell cluster sizes (magic number clusters) we have compared the ico-55 with the hcp-57 cluster and the ico-147 with the hcp-167 cluster. The energies compared in Table 3 always refer to one atom. This is not supposed to be an exhausted DFT analysis since the applicability of DFT is questioned at least for bulk zinc as discussed below. Hence it only shows that DFT predicts a transition from icosahedral structure to hcp structure for very small cluster sizes. One can see that already for $N \geq 13$ the hcp structure is more stable. This is different from the hcp metal magnesium that exhibits icosahedral structure up to $N = 2000$.^{17,55} Compared to DFT calculations, zero-Kelvin calculations with the EAM potential exhibit an overestimation of the icosahedral structure. However, for clusters larger than about 60 atoms the hcp structure becomes more stable in EAM. The EAM potential is fitted to properties at elevated temperatures in order to address particle formation. This can be a reason for a possible shift in the transition from icosahedral to hcp structure compared to DFT, which gives data for zero Kelvin. On the other hand, experimental data rather suggest that icosahedral structure is stable up to roughly $N = 100$.¹⁷ In any case, we use the potential here at elevated temperature and also only for cluster sizes, which are above the transition to hcp obtained from DFT, EAM, as well as from experiments. To verify a possible effect of magic numbers on the structure of the clusters we investigate systems with $N = 13, 55, 57$, and 147 starting at 298.15 K and then cooling down to 50 K. The small ones ($N = 13, 55, 57$) are more stable in icosahedral structure while the bigger one ($N = 147$) is not, which is in agreement with the experiment.¹⁷

2.2 Structure analysis

The common neighbour analysis (CNA) method⁵⁶⁻⁵⁹ is extended here to hcp-surfaces that significantly affect the

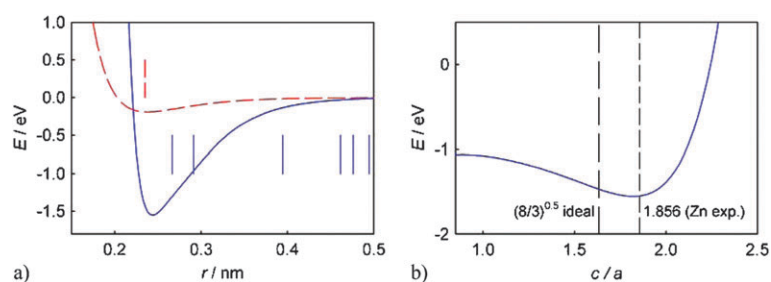


Fig. 2 (a) Cohesive energy E (solid, blue) and the effective pair potential Φ_{eff} (dashed, red) as function of the atomic distance r . The vertical lines mark the coordination shells. (b) Cohesive energy E of the potential model as a function of the c/a -ratio at constant equilibrium distance r_e in the bulk phase. The vertical lines mark the c/a value for an ideal hcp lattice and the experimental value of bulk zinc taken from ref. 53.

Table 3 Energy differences between icosahedral (I_h) and hcp (D_{3h}) structures at zero Kelvin calculated from DFT and EAM. The values are per atoms in a cluster. The magic number clusters for icosahedral structure with 55 atoms and for hcp structure with 57 are compared in the second row

N	$E_B(\text{ico-hcp})$, DFT/eV	$E_B(\text{ico-hcp})$, EAM/eV
13	+0.002	-0.028
55(ico)/57(hcp)	+0.037	-0.007
147(ico)/167(hcp)		+0.0543

properties and growth behaviour of zinc nanoparticles. The CNA is a geometric analysis of the next neighbours of each single atom. In a first step the distance at the first minimum of the pair correlation function is calculated. This CNA cut-off determines whether two atoms are geometrically bound or not. In the second step the number of next neighbours is determined, which means that they are in distance to the central atom less than the CNA cut-off. In the third step the group of common neighbours of the central atom and one of the next-neighbour atoms is determined. Common neighbours are atoms that are closer than the CNA cut-off to the central atom and the chosen next-neighbour. In the fourth step the number of geometric bonds, *i.e.* distances smaller than the CNA cut-off, in the group of next-neighbours is obtained. The final step gives the longest chain of geometric bonds in the group of common neighbours. The result of such analysis is a four-number signature such as 12×421 , *i.e.* 12 next-neighbours, 4 common neighbours with each of the 12 next-neighbours, 2 bonds within the 4 common neighbours, and the longest chain of bonds is 1. This is the signature for the fcc structure. It should be noted that the CNA cut-off can vary during the simulation, especially when the temperature changes or when solidification takes place. This can lead to artificial discontinuities in the amount of recognized structure if the CNA cut-off varies discontinuously. Such effect can be avoided by using a reasonable constant CNA cut-off. In such case the minimum value for the cut-off throughout the simulation run should be used in order to avoid overestimation of ordering. In addition one can also continuously update the CNA cut-off during the simulation or the analysis of the simulation results.

While there are CNA signatures available in the literature for surfaces and edges for many different structures, little is available for the hcp structure. The hcp structure differs from the fcc structure by the order of the layers being ABAB for hcp

and ABCABC for fcc. This has an effect on the distance and hence interaction to the third-next-neighbour for an ideal c/a ratio. While in the bulk phase, fcc and hcp can be distinguished, this is not possible for all surface structures. Surface structures identified as fcc can also be hcp. This is also the case for some icosahedral and decahedral surfaces which both can also be identified as hcp surfaces. In ESI Table 2† the dominant surfaces during the growth of zinc clusters are listed with their CNA signatures. To identify the planes we use the Miller indices and for the hexagonal systems we use the (hkl) notation because it is more descriptive. The corresponding planes are marked in a hcp supercell in Fig. 3a–3c. Fig. 3d–3f show, for example, the three CNA signatures for $(10\bar{1}0)$ plane of the hcp structure. The central atom of the CNA analysis is

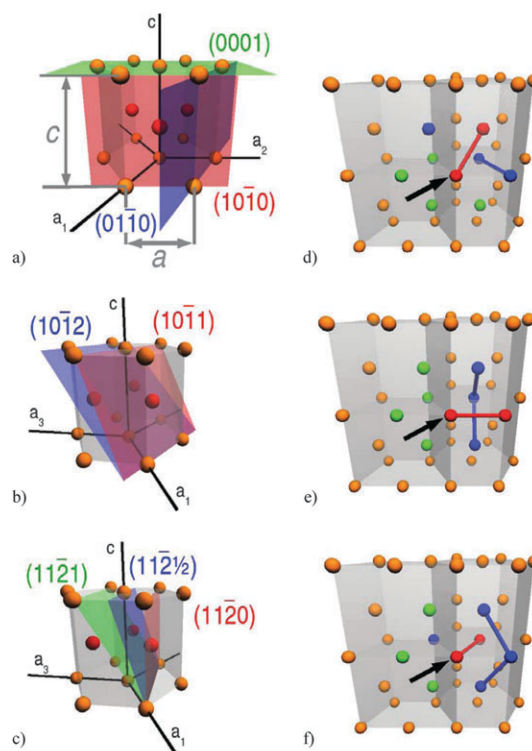


Fig. 3 (a)–(c) A hcp supercell consisting of three unit cells with the planes included in the CNA here. The atoms of the B-layer are coloured (red) different. In (a) the lattice parameter a and c are marked (grey). (d)–(f) CNA signatures for an atom in the A-layer (marked by an arrow) in the $(10\bar{1}0)$ surface of the hcp structure: (d) 311(4), (e) 322(2), and (f) 422(2).

the red one in the middle of the front surface marked by an arrow. It has three types of common neighbours, one in the upper centre part of the right unit cell (Fig. 3d), one in the front plane (Fig. 3e), and one in the centre of the right unit cell in the same horizontal plane as the central atom (Fig. 3f). In order to illustrate ambiguity between hcp and other surfaces we show the CNA analysis of a perfect cubic hcp zinc cluster in Fig. 4. In Fig. 4a the top surface is a $(10\bar{1}0)$ plane being also an icosahedral plane. At the front is a (0001) hcp-plane which is also a (111) fcc plane. At the edges we find some octahedral atoms. If one removes for better visibility the top layer as in Fig. 4b one finds that the second layer is decahedral rather than hcp. So there are two layers in the $(10\bar{1}0)$ hcp-plane before one reaches bulk hcp structure. The reason is that the second layer is below the surface only by a fraction of the lattice constant a and therefore counts to the surface. We call such a layer the B-layer while the first layer is called the A-layer. A $(10\bar{1}0)$ surface hence consists of two layers, the most outer A-layer and, slightly below, the B-layer which both have to be accounted for in the CNA analysis of the surface. The distinction between A- and B-layers is included in the CNA signatures listed in ESI Table 2.† In case of the front (0001) plane the second layer is already below the top plane in the distance of the lattice constant a and hence it has bulk hcp structure. It is therefore not a B-layer.

2.3 Simulation method

The molecular dynamic simulation method and software is described in detail earlier.¹⁰ Briefly, simulations are performed with a leap-frog algorithm using a time step of 2 fs. We have confirmed that this time step conserves the total energy of the system in simulations up to at least 256 ns. In the initial configuration all zinc atoms are placed on a simple cubic lattice with a lattice constant, which is larger than the interaction range of the zinc atoms and yields a homogenous density in the system. This avoids artificially formed clusters at the beginning of the simulation. We have also chosen different initial configurations in order to exclude a possible influence on the particle formation. There is no such influence, which can be easily understood because before nucleation starts the metastable vapour exists for sufficient time (nanoseconds) to

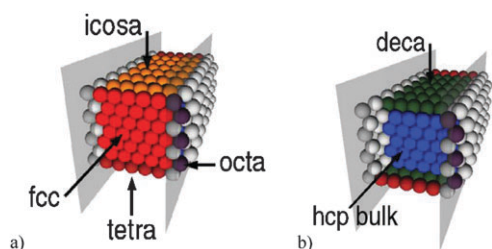


Fig. 4 Ideal hcp cube ($N = 686$) with the lattice parameter of zinc. In (a) the complete cube is shown with periodic boundary conditions perpendicular to the grey planes. The front plane of the cube corresponds to the (0001) - and the top plane to the $(10\bar{1}0)$ -plane of the hcp lattice. These surface planes are additionally in fcc and icosahedral structure with tetrahedral edges. In (b) the top layers are removed for better visibility of the layers below and unique bulk-hcp structure appears below the hcp/fcc structure while an ambiguous hcp/decahedral B-layer appears below the icosahedral top A-layer.

lose any correlation to the initial state. For removing the latent heat during particle formation we add argon as carrier gas. In the long-time limit this corresponds to the NVT ensemble with respect to the zinc system. However, the phenomena of interest appear in the transient period before this limit is reached. Therefore we have a non-equilibrium ensemble being polytropic in thermodynamic terms. The interaction between the argon atoms is modelled with the Lennard-Jones potential using the parameters $\varepsilon_{Ar}/k_B = 120$ K and $\sigma_{Ar} = 0.3405$ nm. Regular Lorentz–Berthelot combining rules are employed for the binary interaction. This requires also Lennard-Jones parameters for zinc. Therefore we have fitted the Lennard-Jones potential to the effective pair potential calculated from the EAM potential. The resulting values are $\varepsilon_{Zn}/k_B = 2204.8$ K and $\sigma_{Zn} = 0.20$ nm. The Lennard-Jones potential is used for zinc only to mimic its interaction with the carrier gas, but not for the zinc–zinc interaction which is modeled by EAM. In order to detect clusters the Stillinger criterion⁶⁰ is employed using a distance value of 0.205 nm, which is 2.5% bigger than the zinc monomer diameter. Atoms closer than this distance belong to a cluster. The suitability of this cluster definition for metal systems has been discussed earlier.¹⁰ The initial velocities are assigned to all atoms at random from a velocity distribution for given temperature. In all simulations presented here we use a Zn : Ar ratio of 1 : 2.

3. Results

Structure

To get a first insight into the structure of the clusters we plot the pair correlation function $g(r)$ of the equilibrated cluster averaged over one nano-second simulation time (500 configurations). Fig. 5a shows the temperature dependence of $g(r)$ for a zinc cluster with 1000 atoms. The radius of this cluster varies from 1.297 nm (400 K) to 1.285 nm (50 K) which roughly limits the range in that $g(r)$ is valid. Typical temperature-dependent behaviour is observed: the peaks become more pronounced and can split into two peaks at low temperature representing the ordered structure of the solid-like state. The dependence of $g(r)$ on the cluster size is shown in Fig. 5b. The structure becomes more pronounced with increasing cluster size which has several reasons: first the melting temperature of a cluster decreases the smaller the clusters are. Small clusters tend towards liquid-like structures while the large clusters tend towards solid-like structures. However, one also has to keep in mind that the valid range of calculating $g(r)$ is limited by the cluster radius, and even peaks closer than the radius are distorted because there are few atoms within the distance of the second and third next neighbour smearing out the peaks. The radii of the different clusters are marked in Fig. 5b in order to get an estimate of the validity of $g(r)$.

For a more detailed insight into the local structure we have performed a CNA analysis of the largest cluster in the system during the growth. This analysis includes icosahedral, octahedral, fcc, and hcp structures for the bulk, as well as surfaces and edges. In Fig. 6 all contributions (bulk, surface, edges) are summarized except for the hcp structure. The hcp structure is separated into bulk and surface structures. In Fig. 6a the CNA

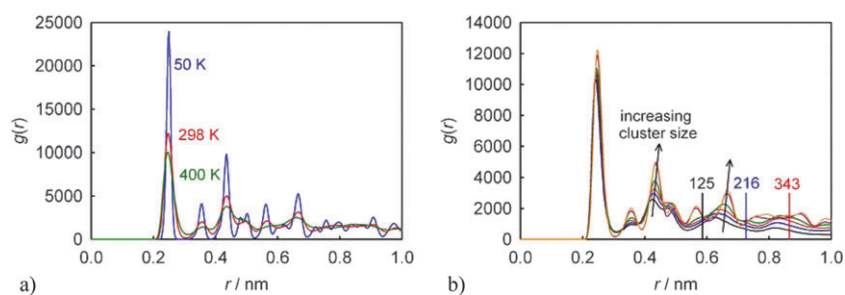


Fig. 5 Pair correlation functions: (a) thermally equilibrated zinc cluster with 1000 atoms at different temperatures; (b) thermally equilibrated zinc cluster of different sizes (125, 216, 343, 512, 729, 1000 atoms) at 298 K. The arrows indicate the sequence with increasing cluster size. The vertical lines mark the radii of the clusters with the indicated number of zinc atoms. The size of the other cluster is larger than 1 nm.

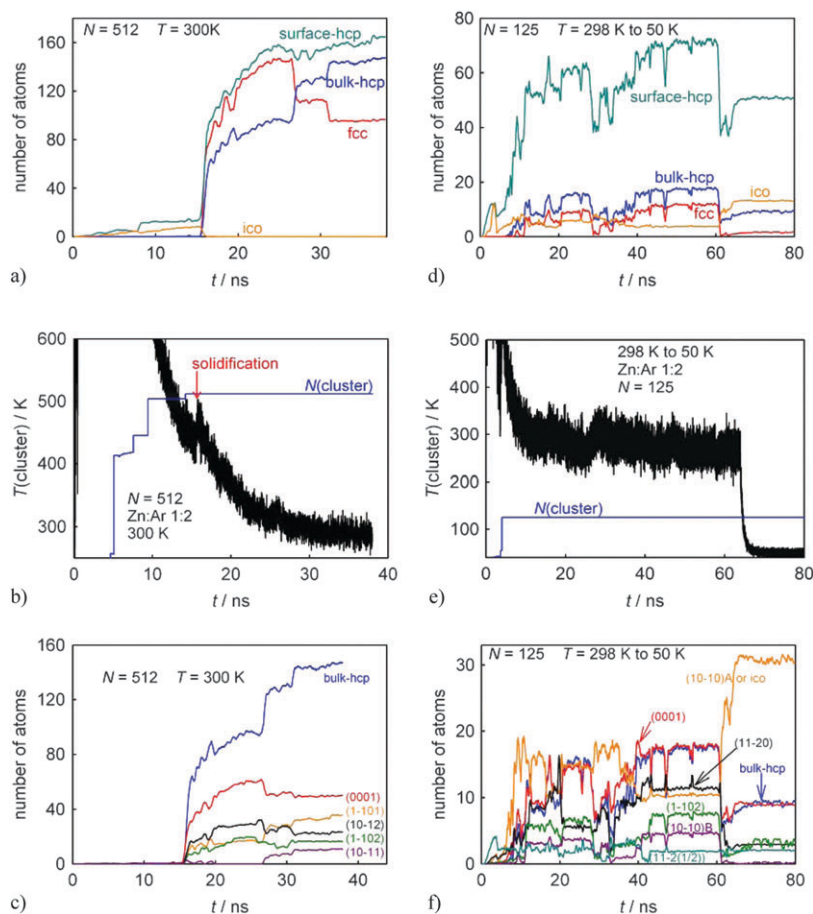


Fig. 6 Structure analysis of the largest cluster by means of CNA during particle formation. (a) CNA of the major structures for a simulation with carrier gas temperature 300 K and 512 zinc atoms. (b) Temperature and size N of the largest cluster corresponding to (a). The final cluster size of 512 atoms is reached at about 15 ns. At about 16 ns the cluster solidifies which is visible by the temperature jump marked by an arrow. (c) CNA analysis of the hcp structures including bulk and the surface structures corresponding to (a). In addition 30 atoms are in vertex hcp structure (not plotted). (d)–(f) As (a)–(c) but for a 125 atom cluster at 298 K and then cooled down to 50 K at 64 ns.

of the largest cluster taken from a simulation with a carrier gas temperature of 300 K is plotted *versus* the simulation time. At about 15 ns the cluster has reached its final size of 512 atoms (Fig. 6b). Solidification takes place at about 16 ns visible by the increasing amount of structure in Fig. 6a and the temperature jump in Fig. 6b caused by the latent heat. In the liquid-like state the cluster mainly consists of disordered structure in the core and small amount of icosahedral-surface and hcp-surface structure. During solidification the icosahedral

structure vanishes while fcc, bulk-hcp, and hcp-surface structures start to form. At the beginning the fcc structure is dominant in the cluster core and later it is transformed partly into bulk-hcp structure in two steps at 27 ns and 31 ns. The amount of surface-hcp structure remains more or less constant. For further analysis of the structure formation we plot in Fig. 6c the contributions to the hcp structure separately. These are bulk-hcp and various surface-hcp structures. After solidification the (0001) surface rapidly becomes dominant and

remains dominant throughout the simulation. Right after solidification the second largest amount of surface atoms is in the $(10\bar{1}2)$ plane. At 27 ns, simultaneously to the reorganisation of the cluster core (Fig. 6a), the number of atoms in the $(10\bar{1}2)$ plane decreases while the $(1\bar{1}01)$ plane becomes the second important surface. At the same time also some atoms in the $(10\bar{1}1)$ plane appear. In Fig. 3b and 3a one can follow the change from the $(10\bar{1}2)$ to the $(10\bar{1}1)$ and finally to the (0001) plane. The $(1\bar{1}01)$ and $(10\bar{1}1)$ planes have more atoms per unit surface area, hence they are energetically more favourable than the $(10\bar{1}2)$ plane. The (0001) plane has the highest atom density per area. It follows that the order of these surfaces at the end of this simulation (Fig. 6e) corresponds to the order of their surface energies. The changes in the surface structure are consistent with the Ostwald step rule, which says that the most-stable phase does not form first, but the one closest in energy.⁶¹ The order of the stability of the different surfaces is similar to that found for zirconium.⁶² For this hcp metal the (0001) surface with the lowest surface energy is dominant followed by the $(1\bar{1}01)$ and the $(1\bar{1}02)$ planes. All other structures included in the investigation (ESI Table 2†) except some vertex- and edge-hcp structures are not present in the zinc clusters simulated here.

We have analyzed the cluster formation for different cluster sizes and observe different kinds of structure development. At the beginning of the particle formation during nucleation and initial growth the temperature is high for all systems and all clusters exhibit liquid-like structure. Most atoms are not in any local order except for a few icosahedral and hcp-surface atoms, which are simply fluctuations. Differences appear after the clusters have grown to their final size. The smallest cluster with 125 zinc atoms remains for a long period of time in disordered liquid-like structure at 298 K (Fig. 6d and 6f). At approximately 61 ns, shortly before the system is cooled down to 50 K at 64 ns, the amount of hcp structure decreases a little bit while the amount of icosahedral structure rises, but the hcp structure still remains dominant. In a set of long-time simulations up to 200 ns at 298 K we find some fluctuations in the structure of the 125 atom cluster which mainly take place in the cluster surface. They are apparently caused by the small energetic difference between the structures compared to $k_B T$. When we cool down the cluster at 58 ns, in a period of the fluctuation where the hcp-surface structure is dominant, we obtain only very few atoms in the icosahedral structure, while most atoms are in hcp-surface and hcp-bulk structure.

In addition a small amount of fcc structure is present at 298 K that almost completely vanishes during restructuring at 61 ns. For the 125 atom cluster the (0001) surface is not dominant especially not after restructuring at 61 ns (Fig. 6f), where the $(10\bar{1}0)$ surface becomes the most important one. The $(10\bar{1}0)$ -hcp structure is also an icosahedral surface structure and does not show up in the 512 atom cluster (Fig. 6c). In contrast, the 512 atom cluster has dominant (0001) -hcp surface structure, which is equivalent to the (111) -fcc surface. On the other hand the $(1\bar{1}01)$ surface being second important in the 512 atom cluster (Fig. 6c) is not present in the 125 cluster (Fig. 6f). Comparison with Table 3 shows that the 125 atom cluster is beyond the transition regime for the icosahedral and hcp structure within the EAM model.

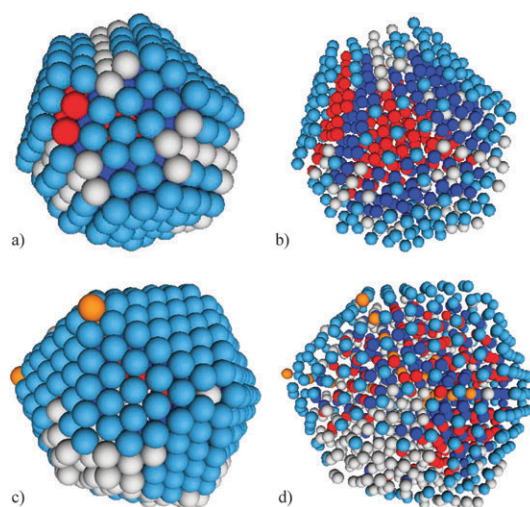


Fig. 7 Snapshots of zinc clusters: (a) 512 atom cluster at 300 K corresponding to 36.5 ns in Fig. 6a–6c. (b) As (a) but with small atom radii in order to show the internal structure. (c) 1000 atom cluster at 50 K and 75.2 ns simulation time. (d) As (c) but with small atom-radii. Although the surfaces look rather ordered one can recognize a disordered region inside the cluster. Legend: (light blue): hcp-surface, (red): fcc, (blue): hcp-bulk, (ochre): icosahedral, light grey: disordered.

Some snapshots of clusters formed in the vapour phase are shown in Fig. 7. The 512 atom cluster in Fig. 7a and 7b corresponds to the simulation in Fig. 6a–6c at 36.5 ns being after the reordering at 27 ns and 31 ns. Most of the surface is in hcp-structure with some atoms in notches cannot be accounted to any order. This is due to the mis-fit of the 512 atom cluster, which does not correspond to a magic-number cluster and therefore hasn't the right amount of atoms to form a closed-shell structure. A look into the interior of the cluster (Fig. 7b) unveils the bulk-hcp and fcc structures. The fcc structure is present as a complete layer, well-visible inside the cluster, followed by a bulk-hcp layer. This is a hint that the remaining fcc structure is caused by stacking faults which may vanish after some further, much longer simulation time. The fact that the clusters at the end of the simulations performed here take transient structures and may not necessarily be in their equilibrium structure is visible in Fig. 7c and 7d. This is a snapshot of a 1000 atom cluster at 50 K. While the surface looks mainly well ordered in Fig. 7c one can recognize a big disordered domain on the left-bottom side inside the cluster in Fig. 7d. This disordered domain is a result of a cluster collision process which has not healed up yet. This cluster is then cooled down to 50 K before this domain is able to form structure in the given period of time. One can detect such partly disordered clusters easily, by the pair correlation function which exhibits liquid-like structure but also by the cluster density as discussed below in the context of Fig. 8d.

Lattice constants and cluster density

In Fig. 8a the next-neighbour distance obtained from the first maximum of the pair correlation function is plotted *versus* the cluster size for three different temperatures. In case of a solid-like cluster this distance corresponds to the lattice constant a . One can observe a trend that the next-neighbour

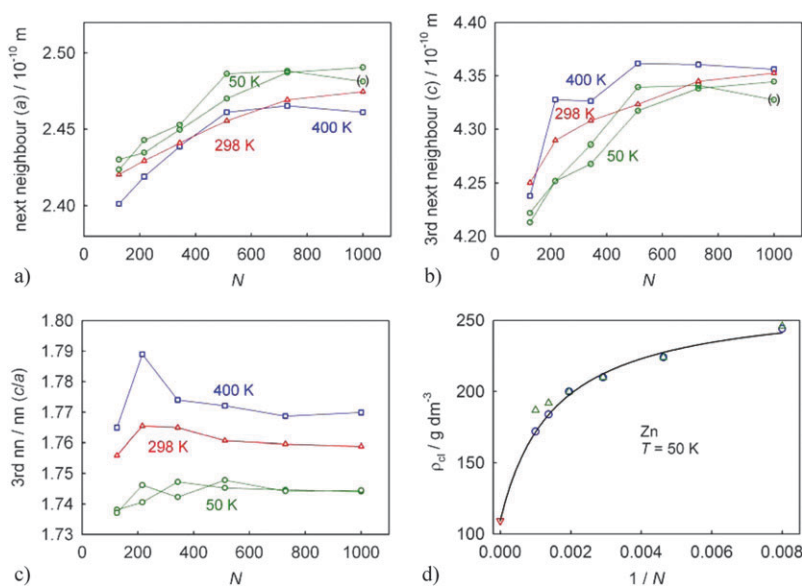


Fig. 8 Location of the first (next neighbour) and third peak (third neighbour) of the pair correlation function. For solid-like clusters these peak positions correspond to the lattice constant a and c respectively. Here all clusters with 343 atoms and smaller ones are liquid-like. The uncertainty of the determination of the distances is 0.02×10^{-10} m. (a) Position of first peak as function of the cluster size for different temperatures. (b) Position of third peak as function of the cluster size for different temperatures. (c) Ratio of the position of the third peak and the first peak (nn = next neighbour). (d) Cluster density plotted *versus* the reciprocal cluster size. The red triangle-down is the experimental value for bulk zinc. The blue circles are from cooling simulations starting at 298 K, the green triangles-up are for cooling simulations starting at 400 K. The solid curve is the correlation with eqn (12).

distance increases with the size of the cluster at all temperatures. This corresponds to a decreasing cluster density with rising cluster size, which agrees with the average cluster density shown in Fig. 8d. This cluster density is calculated from the averaged cluster radius. Fig. 8d shows the results of two simulation series, both cooling down the clusters to 50 K, one starting at 400 K and one starting at 298 K. The obtained densities can be fitted to a simple function including the bulk density of zinc:

$$\rho_{cl} = \rho_{bulk} + \frac{a^3}{b + \frac{1}{N}} \quad (12)$$

The parameters obtained from the fit are $a = 156.9 \text{ g dm}^{-3}$, $b = 1.516 \times 10^{-3}$, with the experimental values of the zinc bulk density $\rho_{bulk} = 109.2 \text{ g dm}^{-3}$. Two data points for the cooling simulations starting at 400 K show some deviations to the other data points. The pair correlation function of the simulation of the 1000 atom cluster ($1/N = 0.001$) does not exhibit typical crystalline structure, which is why its density deviates from the correlation curve. This is also confirmed by the snapshot of this cluster shown in Fig. 7d and discussed above.

The distance to the third neighbour is shown in Fig. 8b. We identify this distance with the lattice constant c in case of solid-like clusters. This distance also increases with the cluster size towards a limiting value. The third-neighbour distance rises with the temperature, however, the temperature dependence is not as systematic as for the next-neighbour distance. One reason is the lower accuracy of the determination of the flat peak maximum. Furthermore, the smaller the cluster the less accurate is the third peak because in small

clusters only few atoms have neighbours in this distance. For the atoms in the two outer shells several third-neighbour atoms are missing due to the cluster surface.

The ratio of the distance to the third-neighbour and the next-neighbour can be identified as the c/a ratio in solid-like clusters. It is plotted in Fig. 8c for different cluster sizes and temperatures. One can see a trend of increasing ratio with increasing temperature. The dependence of this ratio on the cluster size is not as clear and lies within the uncertainty of the data. The average value of all data is 1.76 which lies between the ideal value of 1.63 and the bulk zinc value of 1.86.

The variation of the next- and third-neighbour distances obtained here ranges from 0.24 to 0.25 nm and 0.42 to 0.435 nm respectively for temperatures below 400 K. The next-neighbour distance has been determined before in calculations using a Lennard-Jones model with three-body forces for the Zn_8 cluster (0.2810 nm) and the Zn_{50} cluster (0.2730 nm) at 300 K.²¹ The value for the Zn_{50} cluster may be identified with the lattice constant a , however, 300 K is likely above the melting temperature of the Zn_{50} cluster. Furthermore, the potential model used in that work²¹ consists of a pairwise additive Lennard-Jones potential with an Axilrod–Teller three-body term, which is quite different to the representation of the delocalised electrons in metals.

Doye¹⁹ used the Gupta potential for an investigation of the global energy minimum structures of zinc clusters ranging from the trimer to the 125-mer. In these calculations the c/a ratio of the model is fixed to the bulk value. As a result it was found that at the global minimum, corresponding to zero Kelvin, the structure is qualitative different to the bulk structure; it is based on distorted oblate Marks decahedra. It is also clear that the c/a ratio in a small cluster is not equal to

that in the bulk. The difference between the fcc and the hcp structure appears in the third-neighbour interaction (assuming an ideal c/a ratio of 1.63 without peak splitting) which vanishes with decreasing cluster size. So the hcp structure in small zinc clusters is distorted which means that the c/a ratio can vary. Furthermore, small clusters have a large influence of the surface energy also affecting the lattice constants. Since the potential model developed here reproduces the c/a value (Fig. 2b) for bulk zinc, we think that the deviations of the cluster structure to that in the bulk are realistic and related to effects described above. It should also be noted that properties obtained at the global minimum, *i.e.* at zero Kelvin, are not necessarily comparable to those at finite temperature.

Thermal expansion

It is interesting to note that while the overall thermal expansion is positive (Fig. 8d and 9), as well as the expansion with respect to the third-neighbour distance (c), the next-neighbour distance (a) exhibits a negative thermal expansion. It follows that the model gives an anisotropic thermal expansion and furthermore a negative thermal expansion for the a value at low temperatures (Fig. 8a). This is qualitatively consistent with experimental observations of different authors.^{63,64} They find a negative linear thermal expansion coefficient perpendicular to the c -axis below around 80 K. Since we here have only data points at 400 K, 298 K, and 50 K we have not determined a transition temperature between positive and negative thermal expansion. The c/a ratio decreases by about 2 per cent from 273 K to 0 K.⁶⁴ This is in the order of magnitude that we find for zinc clusters with the EAM model (Fig. 8c).

It is very difficult to determine the exact melting point from the plot of the cluster radius *versus* the temperature, nevertheless one can recognize two domains (Fig. 9a and 9b). The structure analysis by CNA shows a distinct increase of structure when passing from the high-temperature to the low-temperature domain. Thus, the low-temperature domain can be identified with a structured solid-like state and the high-temperature domain with a liquid-like state. From the regression of the simulation data one obtains the linear thermal expansion coefficient α :

$$\alpha = \frac{1}{r_{\text{cl}}} \left(\frac{\partial r_{\text{cl}}}{\partial T} \right) \quad (13)$$

For small clusters (Fig. 9a) the fluctuations are larger than for big clusters (Fig. 9b), which leads to a larger uncertainty in α . This uncertainty is even larger in the high-temperature domain than at low temperatures especially for small clusters with 216 atoms and less. Still, one can recognize a weak trend towards decreasing thermal expansion with the cluster size in Fig. 9c. This also means that the thermal expansion decreases with decreasing cluster density. The experimental values for the thermal expansion in zinc single crystalline bulk at 298 K are added in Fig. 9c for the two lattice constants separately.⁶⁵ The average values obtained in both temperature domains are located between the thermal expansion coefficients of the experimental values for the two lattice constants.

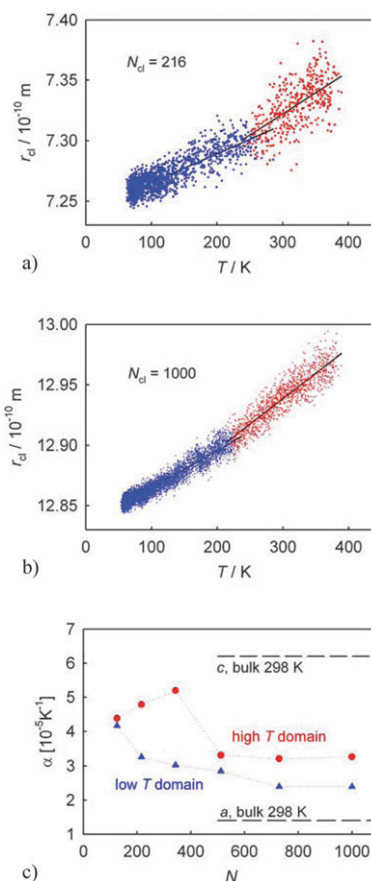


Fig. 9 Cluster radii as function of the temperature obtained from cooling simulations. (a) Cluster size: 216. The data points are divided in a low and a high temperature group. (b) Cluster size: 1000. (c) Reduced linear thermal expansion coefficient (eqn (13)) for different cluster sizes. The low temperature values are taken from two simulations.

4. Conclusions

We have developed an EAM potential model for the hcp metal zinc using experimental data for the bulk properties and for the zinc dimer as well as the Hartree–Fock electron distributions functions. The screening function of the core repulsion by delocalised electrons is calculated by integration over the electron distribution rather than by fitting to experimental data. This model is capable of describing the hcp structure of zinc in the bulk phase as well as in small clusters. For small clusters we find a c/a ratio midway between the zinc bulk c/a ratio and the value for c/a ratio of the ideal closed packed hcp structure. During cluster growth from supersaturated vapour at elevated temperature, the clusters take transient icosahedral/hcp structures in the surface, which eventually transform completely into hcp structure. The core of the cluster is mainly in the hcp structure during growth. The hcp-surface structures are ambiguous and belong also to icosahedral surface structures for small clusters ($N < 60$) and to fcc structures for large clusters. One can observe that for small clusters the icosahedral surface structure remains more stable. For larger clusters the amount of icosahedral

structure present in the liquid-like state completely vanishes after solidification.

Experimental investigations of zinc and magnesium clusters have shown that for cluster sizes below $N = 100$ the mass spectra of both metals look very similar with few exceptions and are consistent with an icosahedral structure.¹⁷ From DFT calculations one learns that magnesium clusters are icosahedral up to $N = 2000$,⁵⁵ and experimental investigations confirm these results at least up to $N = 1415$.¹⁷ Hence, the small zinc clusters up to roughly $N = 100$ are also expected to be icosahedral, which is in agreement with our EAM results in the sense that we find an icosahedral Zn₅₅ cluster more stable than the hcp cluster at zero Kelvin (Table 3). At elevated temperature we still find a small amount of icosahedral structure for $N = 125$ in the surface. Concerning the difference between the experiment and DFT calculations it should be noted that the accuracy of DFT for zinc, at least for bulk phase, has been questioned recently.⁶⁶ Hence, the transition from icosahedral to hcp below $N = 13$ (Table 3) may be inaccurate. It should rather be understood as a hint that the transition from icosahedral to hcp structure is at much smaller cluster size than for magnesium. This might be related to the fact that the c/a ratio is almost ideal for bulk magnesium while it is very different for bulk zinc. In experiments¹⁷ no indication of icosahedral structure beyond $N = 100$ up to $N = 165$ has been found, especially no magic number cluster with $N = 147$ has been found for zinc. The magic numbers in the mass spectrum could not be explained by a geometrical model. The results obtained here from the EAM calculations suggest that a combination of the hcp structure with some icosahedral surface structure may be an alternative explanation. These structures are mixed and hence may give other stable cluster sizes. An attempt to explain the mass spectra of zinc by assuming tetrahedral clusters has shown that such geometry is not stable for zinc clusters with $N > 4$.⁶⁷ It has been found to be more stable for cadmium clusters but this is due to relativistic effects which are important for cadmium but not for zinc.⁶⁷ The EAM potential is consistent with this results; the Zn₁₀ tetrahedral pyramid is more than 0.1 eV per atom less stable than the Zn₁₃ icosahedral or hcp structure. These authors leave amorphous or low-symmetry clusters to explain the mass spectra of zinc; mixed structures may be another possibility.

Thermal expansion coefficients obtained with our model correspond to the average of the experimental thermal expansion coefficients of the two lattice constants in bulk zinc. While it is difficult to obtain the anisotropic thermal expansion from the different directions in a cluster lattice we have used the first and third peak of the pair correlation function to estimate the lattice constants in solid-like clusters. Although this estimation is not very accurate we have found a clear and systematic dependence of the lattice constants on the size and qualitatively the anisotropic thermal expansion of the lattice constants as observed experimentally.

Acknowledgements

This work has been partly supported by the German Research Foundation.

References

- 1 D. D. McBride and P. M. Sherman, *AIAA J.*, 1972, **10**, 1058.
- 2 O. Daub, W. Langel, C. Reiner and L. Kienle, *Ber. Bunsen-Ges. Phys. Chem.*, 1997, **101**, 1753.
- 3 F. Rataboul, C. Nayral, M.-J. Casanove, A. Maisonnat and B. Chaudret, *J. Organomet. Chem.*, 2002, **643–644**, 307.
- 4 Ph. Buffat and J.-P. Borel, *Phys. Rev. A*, 1976, **13**, 2287.
- 5 D. Schebarchov and S. C. Hendy, *Phys. Rev. Lett.*, 2006, **96**, 256101.
- 6 Y. G. Chushak and L. S. Bartell, *J. Phys. Chem. B*, 2003, **107**, 3747.
- 7 N. Lümmer and T. Kraska, *Phys. Rev. B*, 2008, **77**, 045425.
- 8 M. Tomonari, H. Tatewaki and T. Nakamura, *J. Chem. Phys.*, 1984, **80**, 344.
- 9 S. C. Hendy and J. P. K. Doye, *Phys. Rev. B*, 2002, **66**, 235402.
- 10 F. Römer and T. Kraska, *J. Chem. Phys.*, 2007, **127**, 234509.
- 11 A. Steinfeld, *Int. J. Hydrogen Energy*, 2002, **27**, 611.
- 12 M. Karlsson, I. Alxneit, F. Rütten, D. Wuillemin and H. R. Tschudi, *Rev. Sci. Instrum.*, 2007, **78**, 034102.
- 13 H.-J. Flad, F. Schautz, Y. Wang, M. Dolg and A. Savin, *Phys. J. D*, 1999, **6**, 243.
- 14 J. Wang, G. Wang and J. Zhao, *Phys. Rev. A*, 2003, **68**, 013201.
- 15 W. Schroeder, H. Wigggenhauser, W. Schrittenlacher and D. M. Kolb, *J. Chem. Phys.*, 1987, **86**, 1147.
- 16 O. Kostko, G. Wrigge, O. Cheshnoversusky and B. v. Issendorf, *J. Chem. Phys.*, 2005, **123**, 221102.
- 17 Th. Diederich, T. Döppner, Th. Fennel, J. Tiggesbäumker and K.-H. Meiwes-Broer, *Phys. Rev. A*, 2005, **72**, 023203.
- 18 R. Ramprasad and R. G. Hoagland, *Model. Simul. Mater. Sci. Eng.*, 1993, **1**, 189.
- 19 J. P. K. Doye, *Phys. Rev. B*, 2003, **68**, 195418.
- 20 M. Igarashi, M. Khantha and V. Vitek, *Philos. Mag. B*, 1991, **63**, 603.
- 21 L. Amirouche and S. Erkoç, *Phys. Rev. A*, 2003, **68**, 043203.
- 22 J. A. Nuth, K. A. Donnelly, B. Donn and L. U. Lilleleht, *J. Chem. Phys.*, 1986, **85**, 1116.
- 23 M. M. Rudek, J. L. Katz and H. Uchtmann, *J. Chem. Phys.*, 1999, **110**, 11505.
- 24 N. Lümmer and T. Kraska, *J. Aerosol Sci.*, 2005, **36**, 1409.
- 25 N. Lümmer and T. Kraska, *Nanotechnology*, 2005, **16**, 2870.
- 26 H. J. Freund and S. H. Bauer, *J. Chem. Phys.*, 1977, **81**, 994.
- 27 D. J. Oh and R. A. Johnson, *J. Mater. Res.*, 1988, **3**, 471.
- 28 M. S. Daw and M. I. Baskes, *Phys. Rev. Lett.*, 1983, **50**, 1285.
- 29 M. S. Daw and M. I. Baskes, *Phys. Rev. B*, 1984, **29**, 6443.
- 30 S. M. Foiles, M. S. Daw and M. I. Baskes, *Phys. Rev. B*, 1986, **33**, 7983.
- 31 V. G. Grigoryan and M. Springborg, *Phys. Chem. Chem. Phys.*, 2001, **3**, 5135.
- 32 S. Chen, J. Xu and H. Zhang, *Comput. Math. Sci.*, 2004, **29**, 428.
- 33 D. Schebarchov and S. C. Hendy, *Phys. Rev. B*, 2006, **73**, 121402.
- 34 V. G. Grigoryan, D. Alamanova and M. Springborg, *Phys. Rev. B*, 2006, **73**, 115415.
- 35 Y. H. Chui, G. Grochola, I. K. Snook and S. P. Russo, *Phys. Rev. B*, 2007, **75**, 033404.
- 36 K. O. E. Henriksson, K. Nordlund and J. Keinonen, *Phys. Rev. B*, 2007, **76**, 245428.
- 37 B. Medasani, Y. H. Park and I. Vasiliev, *Phys. Rev. B*, 2007, **75**, 235436.
- 38 E. Clementi and C. Roetti, *Roothaan–Hartree–Fock Atomic Wavefunctions. Atomic Data and Nuclear Data Tables*, 1974, **14**, 167.
- 39 K. Iokibe, H. Tachikawa and K. Azumi, *J. Phys. B*, 2007, **40**, 427.
- 40 U. Wedig, M. Jansen, B. Paulus, K. Rosciszewski and P. Sony, *Phys. Rev. B*, 2007, **75**, 205123.
- 41 P. Brommer, F. Gähler and H.-R. Trebin, *Force Matching—Grundlagen und erste Ergebnisse*, SFB 382 Report 205, 2004.
- 42 K. W. Jacobson, J. K. Norskov and M. J. Puska, *Phys. Rev. B*, 1987, **35**, 7423.
- 43 R. A. Johnson, *Phys. Rev. B*, 1972, **6**, 2094.
- 44 M. S. Daw, *Phys. Rev. B*, 1989, **39**, 7441.
- 45 J. H. Rose, J. R. Smith, F. Guinea and J. Ferrante, *Phys. Rev. B*, 1984, **29**, 2963.
- 46 R. A. Johnson, *Phys. Rev. B*, 1988, **37**, 3924.
- 47 M. J. Puska, R. M. Nieminen and M. Manninen, *Phys. Rev. B*, 1981, **24**, 3037.

- 48 R. Drautz and D. G. Pettifor, *Phys. Rev. B*, 2006, **74**, 174117.
- 49 X. D. Dai, Y. Kong, J. H. Li and B. X. Liu, *J. Phys.: Condens. Matter*, 2006, **18**, 4527.
- 50 A. F. Voter, *Los Alamos Technical Report LA-UR 93-3901*, Los Alamos National Laboratory, 1993.
- 51 L. Fast, J. M. Wills, B. Johansson and O. Eriksson, *Phys. Rev. B*, 1995, **51**, 17431.
- 52 W. B. Pearson, *Handbook*, Oxford, Pergamon, 1967.
- 53 M. D. Morse, *Chem. Rev.*, 1986, **86**, 1049.
- 54 B. Wittich and U. K. Deiters, *Phys. Chem. Chem. Phys.*, 2009, submitted.
- 55 A. Köhn, F. Weigend and R. Ahlrichs, *Phys. Chem. Chem. Phys.*, 2001, **3**, 711.
- 56 J. D. Honeycutt and A. C. Andersen, *J. Phys. Chem.*, 1987, **91**, 4950.
- 57 A. S. Clarke and H. Jónsson, *Phys. Rev. E*, 1993, **47**, 3975.
- 58 D. Faken and H. Jónsson, *Comput. Math. Sci.*, 1994, **2**, 279.
- 59 N. Lümnen and T. Kraska, *Model. Simul. Mater. Sci. Eng.*, 2007, **15**, 319.
- 60 F. H. Stillinger, *J. Chem. Phys.*, 1963, **38**, 1486.
- 61 W. Ostwald, *Z. Phys. Chem.*, 1897, **22**, 289.
- 62 G. J. Ackland, S. J. Wooding and D. J. Bacon, *Philos. Mag. A*, 1995, **71**, 553.
- 63 E. Grüneisen and E. Göens, *Z. Phys.*, 1924, **29**, 141.
- 64 R. W. Meyerhoff and J. F. Smith, *J. Appl. Phys.*, 1962, **33**, 219.
- 65 H. M. Gilder and G. N. Wallmark, *Phys. Rev.*, 1969, **182**, 771.
- 66 N. Gaston, B. Paulus, U. Wedig and M. Jansen, *Phys. Rev. Lett.*, 2008, **100**, 226404.
- 67 M. P. Johansson and P. Pyykkö, *Phys. Chem. Chem. Phys.*, 2004, **6**, 2907.
- 68 M. J. Bacon and J. W. Martin, *Philos. Mag. A*, 1981, **63**, 603.